Carbon 146 (2019) 513–523

Contents lists available at ScienceDirect

Carbon

journal homepage: www.elsevier.com/locate/carbon

In situ green reduced graphene oxide functionalized 3D printed scaffolds for bone tissue regeneration

Cátia S.D. Cabral [a], Sónia P. Miguel [a], Duarte de Melo-Diogo [a], Ricardo O. Louro [b], Ilídio J. Correia [a, c, *]

[a] CICS-UBI – Centro de Investigação em Ciências da Saúde, Universidade da Beira Interior, Av. Infante D. Henrique, 6200-506, Covilhã, Portugal
[b] ITQB – Instituto de Tecnologia Química e Biológica António Xavier, Universidade Nova de Lisboa, 2780-157, Oeiras, Portugal
[c] CIEPQPF – Departamento Engenharia Química, Universidade de Coimbra, Rua Silvio Lima, 3030-790, Coimbra, Portugal

ARTICLE INFO

Article history:
Received 23 October 2018
Received in revised form
21 December 2018
Accepted 30 January 2019
Available online 6 February 2019

Keywords:
3D scaffolds
Bone tissue engineering
Green chemistry
Rapid prototyping
Reduced graphene oxide

ABSTRACT

The incorporation of reduced graphene oxide (rGO) nanomaterials into scaffolds structure can be explored to enhance the properties of these 3D matrices in bone regeneration applications. However, the weak water solubility and poor colloidal stability of rGO have hindered its incorporation in blends aimed to produce scaffolds by 3D printing. Furthermore, rGO is generally obtained by treating graphene oxide (GO) with hydrazine hydrate, which is a highly hazardous reducing agent. To overcome these problems, herein a novel environmentally-friendly method was developed to assemble 3D printed scaffolds incorporating rGO. Such was achieved through the *in situ* reduction mediated by L-Ascorbic acid of the GO already present on tricalcium phosphate/gelatin/chitosan scaffolds. The scaffolds functionalized with rGO through the *in situ* method (TGC_irGO) displayed enhanced wettability and improved mechanical properties without impairing their porosity when compared to their equivalents functionalized with GO and non-functionalized scaffolds (TGC_GO and TGC, respectively). Moreover, the TGC_irGO scaffolds displayed an improved calcium deposition at their surface and an enhanced alkaline phosphatase (ALP) activity, along 21 days of incubation. Additionally, scaffolds also displayed antimicrobial activity without compromising osteoblasts' viability and proliferation. Such features reveal the potential of the TGC_irGO scaffolds for bone tissue regeneration applications.

1. Introduction

Graphene oxide (GO) is a 2D material composed of an oxygenated graphitic lattice [1]. This material has been showing promising properties for application in widespread biomedical areas such as drug/gene delivery, biological sensing, imaging and tissue engineering [2–4]. Particularly, the use of GO in bone tissue regeneration applications is very appealing since the incorporation of this material into scaffolds' structure can improve their physicochemical and mechanical properties [5–7]. Furthermore, scaffolds functionalized with GO can induce the differentiation of stem cells to osteoblasts and also improve the biomineralization process, rendering them a remarkable potential for bone healing applications [7]. Moreover, the water solubility of GO, arising from its oxygen-functional groups (hydroxyl, carboxyl and epoxy) [8], allows the preparation of blends containing this nanomaterial with adequate properties for being processed by 3D printing techniques [5,9]. This is of paramount importance since 3D printed scaffolds can display a controlled composition capable of mimicking the organic/inorganic phases of the native bone as well as an adjustable architecture to the injured site [5,10]. In this way, scaffolds produced by 3D printing offer distinctive advantages when compared to those produced by other techniques such as freeze-drying, phase separation or gas foaming [11].

Despite of the excellent properties of GO, the reduction of this material (a process that intends to restore its graphitic lattice by removing the oxygen-functional groups) can further enhance its mechanical properties and osteogenic potential [12]. In fact, Kanayama et al. revealed that collagen scaffolds coated with reduced graphene oxide (rGO) display a greater compressive strength, a higher calcium adsorption and a stronger induction of the alkaline phosphatase activity, when compared to their

* Corresponding author. CICS-UBI – Centro de Investigação em Ciências da Saúde, Universidade da Beira Interior, Av. Infante D. Henrique, 6200-506, Covilhã, Portugal.
E-mail address: icorreia@ubi.pt (I.J. Correia).

https://doi.org/10.1016/j.carbon.2019.01.100
0008-6223/

equivalents containing GO [13]. However, the direct incorporation of rGO in 3D printed scaffolds possesses some challenges. Due to the physico-chemical changes induced by the reduction process, rGO usually displays a weak water solubility and a poor colloidal stability, leading to its rapid aggregation in aqueous solutions [14]. This phenomenon hinders the preparation of rGO-containing blends with suitable processability for 3D printing. Furthermore, rGO is generally attained by treating GO with hydrazine hydrate, which is a highly hazardous reducing agent [15]. To surpass such drawbacks, developing an environmentally-friendly method that allows the reduction of the GO already incorporated on 3D printed scaffolds (*in situ* reduction) is an appealing strategy to overcome the safety and aggregation problems associated with the direct incorporation of rGO. Furthermore, such method should not compromise the structure of the 3D printed scaffolds as well as scaffolds' architecture.

Herein, a blend of tricalcium phosphate/gelatin/chitosan/GO was used to print the 3D scaffolds, that were subsequently immersed in L-Ascorbic acid (LAA; Vitamin C) under mild conditions (40 °C for 24 h), to reduce the GO present within the printed scaffolds (TGC_irGO). LAA was selected as the reducing agent since it is a natural compound with good biocompatibility [16]. Moreover, tricalcium phosphate (TCP) was used to mimic the inorganic phase of the bone due to its bioactivity and osteoconductivity. Gelatin (Gel) and Chitosan (CH) were selected to reproduce bone's organic phase due to their biocompatibility, bioadhesivity, wettability and antimicrobial activity [17,18]. In addition, the mild conditions used during the printing and GO reduction processes assured that the structure of the scaffolds remained intact. The results revealed that TGC_irGO scaffolds presented an enhanced wettability and mechanical properties, while their porosity remains similar to that exhibited by their equivalents functionalized with GO and non-functionalized scaffolds (TGC_GO and TGC, respectively). Moreover, the TGC_irGO scaffolds displayed an improved calcium deposition at their surface and were able to augment the alkaline phosphatase (ALP) activity, along 21 days of incubation. Additionally, scaffolds also exhibited antimicrobial properties against *S. aureus* and *E. coli*, without compromising the viability and proliferation of osteoblast cells. Such features highlight the potential of the TGC_irGO scaffolds for bone tissue regeneration applications.

2. Materials and methods

2.1. Materials

Alizarin Red S, alkaline phosphatase, chitosan medium molecular weight (190 000–310 000 Da; degree of deacetylation: 83.35% ± 0.23), Dulbecco's modified Eagle's medium (DMEM-F12), ethylenediaminetetraacetic acid (EDTA), diethanolamine, gelatin 160 bloom, glutaraldehyde 25% (v/v), LB broth, hydrochloric acid (HCl), *p*-Nitrophenylphosphate (pNPP), paraformaldehyde (PFA), phosphate buffered saline solution (PBS), sodium hydroxide (NaOH), sodium tripolyphosphate (TPP), Triton X-100 and trypsin were purchased from Sigma-Aldrich (Sintra, Portugal). Graphene oxide (GO) was obtained from NanoPoz (Umultowska Poznan, Wielkopolska). Lysozyme from chicken egg was acquired from Alfa Aesar (Haverhill, MA, USA). Acetic acid was acquired from Pronalab (Barcelona, Spain). Normal human osteoblast (hOB; 406-05f) cryopreserved cells were bought from Cell Applications, Inc. (San Diego, USA). *Staphylococcus aureus* clinical isolate (*S. aureus*; ATCC 25923) and *Escherichia coli DH5a* (*E. coli*) were used to evaluate antimicrobial properties of scaffolds. Fetal bovine serum was provided by Biochrom AG (Berlin, Germany). 3-(4,5-dimethylthiazol-2-yl)-5-(3-carboxymethoxyphenyl)-2-(4-sulfophenyl)-2H-tetrazolium (MTS) was bought from Promega (Madison, WI, USA). Propidium Iodide buffer was acquired from Life Technologies (Maryland, USA). Tris base and L-Ascorbic acid (LAA) were obtained from Fisher Scientific (Porto Salvo, Portugal). Tricalcium phosphate (TCP) was purchased from Panreac (Barcelona, Spain). Double deionized and filtered water was obtained using a Milli-Q Advantage A10 ultrapure Water Purification System (0.22 μm filtered; 18.2 MΩ/cm at 25 °C).

2.2. Methods

2.2.1. Production of TGC_irGO scaffolds

TCP and the Gel/CH were combined at an approximate ratio of 80/20 (w/w) to produce the TGC_irGO scaffolds (Fig. 1A). Initially, the CH (800 mg in 15 mL of acetic acid solution (1% (v/v)) and Gel (150 mg in 1 mL of water at 50 °C) solutions were thoroughly mixed, by using an X10/25 Ultra-turrax. Afterwards, the TCP (4800 mg) and GO (16 mg) were added to the CH/Gel solution. Then, this solution was homogenized for 30 min by using an X10/25 Ultra-turrax. Subsequently, the TCP/Gel/CH/GO solution was loaded into a syringe (10 cc Luer Lock) and extruded by a Fab@Home 3D printer in order to produce the scaffolds (Fig. 1A). After the printing process, each scaffold (n = 9) was treated with LAA (10 mM; 6 mL) at 40 °C for 24 h (30 rpm) – *in situ* green reduction. Subsequently, the scaffolds were crosslinked through their immersion in a sodium tripolyphosphate (TPP) solution (10% (w/v)) for 48 h and air-dried at Room Temperature (RT) overnight, yielding TGC_irGO scaffolds.

For comparative purposes, TGC_GO and TGC scaffolds were also produced. The TGC_GO scaffolds were produced following the above described protocol but were not subjected to the *in situ* reduction method. In turn, the TGC scaffolds were also produced as described above but did not incorporate GO and were not subjected to the *in situ* reduction process. The methodologies used for the characterization of the morphological and physico-chemical properties of the produced scaffolds are described in the Supplementary Information.

2.2.2. Characterization of the biological properties of the produced scaffolds

2.2.2.1. Characterization of cell viability and proliferation in the presence of the produced scaffolds. The cytotoxic profile of the scaffolds towards normal human osteoblast (hOB) cells was evaluated through the MTS assay [5]. In brief, different scaffolds' formulations were cut into small pieces, placed into 96-well plates and then sterilized under UV radiation for 1 h. Subsequently, hOB cells were seeded in contact with the scaffolds at a density of 10×10^3 cells/well. After 1, 3 and 7 days of incubation, the medium was removed, and cells were incubated with 120 μL of fresh medium containing MTS (20 μL) for 4 h (37 °C, 5% CO_2). Then, the absorbance of the samples was measured at 490 nm, using a microplate reader (Bio-Rad xMark microplate spectrophotometer). Cells incubated without the materials were used as the negative control (K^-), while cells incubated with EtOH (70%) were used as the positive control (K^+).

2.2.2.2. Characterization of cell adhesion at the surface of the scaffolds. Cell adhesion at the surface of the scaffolds was evaluated by Scanning Electron Microscopy (SEM). In brief, hOB cells were seeded (40×10^3 cells/well) in contact with the scaffolds. After 1, 3 and 7 days of incubation, the samples were washed and fixed with glutaraldehyde (2.5% (v/v)) for 30 min. Then, the samples were frozen at −80 °C, freeze-dried for 3 h and prepared for SEM analysis (as described in Section 1.2 of Supplementary Information).

2.2.2.3. Confocal microscopic analysis. The cell distribution within

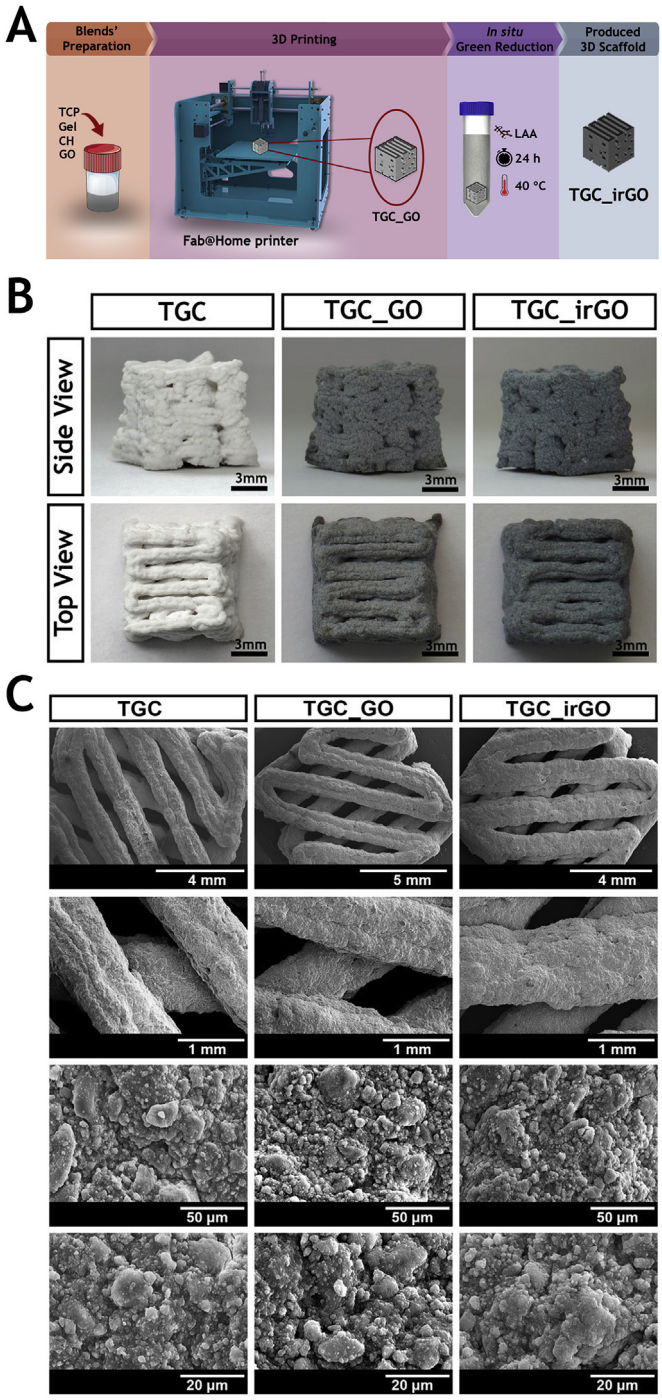

Fig. 1. Production and characterization of 3D scaffolds. Schematic representation of experimental setup used to produce the TGC_irGO scaffolds (A); representative macroscopic images of the different scaffolds produced (side and top views) (B) and SEM images (at different magnifications) showing the morphology and surface topography of the produced 3D scaffolds (C). (A colour version of this figure can be viewed online.)

the scaffolds was characterized through confocal laser scanning microscopy (CLSM). In brief, hOB cells (40×10^3 cells/well) were seeded in the presence of scaffolds in µ-Slide 8-well Ibidi imaging plates (Ibidi GmbH, Germany) [18]. After 72 h, the samples were treated with a permeabilization solution (Triton X-100) and the cell nucleus was labelled with propidium iodide (PI; 15 mM) during 15 min at 37 °C. Then, the samples were washed with PBS and fixed with 4% PFA, for 15 min, at RT. Imaging experiments were then performed in a Zeiss LSM 710 laser scanning confocal microscope (Carl Zeiss SMT Inc., USA), where consecutive z-stacks were acquired. 3D reconstruction and image analysis were performed in Zeiss Zen 2010 [19].

2.2.2.4. Alizarin Red S (ARS) staining. The capacity of scaffolds to promote calcium deposition by hOB cells was evaluated through an ARS staining method, following a protocol previously optimized by our group [5]. Briefly, cells were seeded (10×10^2 cells/well) in contact with the scaffolds (n = 6) in 6-well plates. After 1, 3, 7, 14 and 21 days of incubation, the samples were fixed with 4% PFA during 1 h. Afterwards, samples were stained with 1 mL of ARS (40 mM, pH = 4.2) during 1 h, under gentle shaking. Subsequently, the samples were washed twice with deionized H_2O to remove the excess of ARS. Then, microscopic images were acquired to visualize the calcium deposits produced by hOB cells in contact with the scaffolds.

Then, the ARS adsorbed on scaffolds was quantified by eluting it with acetic acid (1 mL; 10% (v/v)) under shaking for 30 min. Thereupon, the samples were vortexed for 30 s and the liquid phase was heated at 85 °C for 10 min. Afterwards, the samples were centrifuged at 14 000 g, for 25 min and at RT, followed by neutralization of the supernatant (500 µL) with ammonium hydroxide (200 µL; 10% (v/v)). Finally, the absorbance was determined at 405 nm using a microplate reader (Biorad xMark microplate spectrophotometer). The ARS concentration was then determined using a standard curve.

2.2.2.5. Alkaline phosphatase (ALP) activity and dsDNA quantification. The ALP activity of hOB cultured in contact with 3D scaffolds was evaluated as described elsewhere [19]. In brief, hOB cells were cultured in the presence of the scaffolds during 1, 3, 7, 14 and 21 days (as described in Section 2.2.2.1). Afterwards, samples were treated with Triton X-100 (1 mL) and a cell scraper was used to remove the cell-scaffolds constructs, which were then transferred into microtubes. Thereafter, the samples were subjected to a freeze-thaw cycle and sonicated for 15 min to promote cells' lysis. Afterwards, the samples were centrifuged (14 000 g, 15 min, at RT) and the supernatant was collected to quantify the ALP activity and the dsDNA content.

The ALP activity was determined by incubating the samples' supernatant (20 µL) with 60 µL of a substrate solution (0.2% *p*-Nitrophenylphosphate (pNPP) (w/v) in 1 M diethanolamine HCl, at pH 9.8) for 45 min, at 37 °C, in the dark. Subsequently, 80 µL of the stop solution (NaOH (2 M) containing EDTA (0.2 mM)) was added. Then, the production of *p*-nitrophenol was evaluated by measuring the absorbance at 405 nm. The ALP activity was determined according to the protocol provided by the manufacturer.

The total DNA content was quantified using the Quant-iT PicoGreen Kit (Invitrogen, Carlsbad, CA) as recommended by the manufacturer. Briefly, 100 µL of the PicoGreen reagent (1:200 dilution of the PicoGreen reagent in 1X TE Buffer) was incubated with an equal volume of the cell's lysate for 5 min, in the dark. Afterwards, the fluorescence was measured in a microplate reader using an excitation and emission wavelengths of 485 and 535 nm, respectively. Samples' dsDNA content was then determined by using a standard curve.

2.2.3. Evaluation of the bactericidal activity of the scaffolds

S. aureus and *E. coli*, gram-positive and gram-negative bacteria, were used to characterize the antibacterial activity of the scaffolds. For this purpose, a modified Kirby-Bauer technique was used [10]. In brief, 200 µL of the bacteria medium (at a concentration of 1×10^8 CFU/mL) were dispensed onto an agar plate. Circular

scaffolds (n = 3) were then placed on the agar plate and incubated during 24 h at 37 °C. Afterwards, the inhibitory halos around the samples were photographed and their diameters were measured using the *ImageJ* software. The bacteria growth at the surface of the scaffolds was also confirmed by SEM analysis (samples were prepared as described in Section 1.2. of the Supplementary Information).

2.2.4. Statistical analysis

One-way analysis of variance (ANOVA) with the Newman-Keuls post hoc test was used for the analysis of the obtained results. A p value lower than 0.05 ($p < 0.05$) was considered statistically significant.

3. Results and discussion

3.1. Characterization of the morphology of the scaffolds

The fabrication process used to produce the TGC_irGO scaffolds is schematically represented in Fig. 1A. First, a homogeneous mixture of TCP (an inorganic compound), Gel, CH (organic elements) and GO was deposited layer-by-layer, resulting in the production of the 3D scaffolds that mimic the natural bone matrix composition (20–30% organic, 70–80% inorganic) [10,20]. In this case, TCP confers mechanical and osteogenic properties to the scaffolds [21]. On the other hand, Gel and CH provide bioadhesive and antibacterial properties, respectively [17,18]. Then, the environmentally-friendly *in situ* reduction of the GO incorporated within the scaffolds was performed by immersing the 3D matrices in a solution containing LAA, for 24 h, at 40 °C. By employing this novel approach, it was possible to overcome the problems associated with the inclusion of rGO into 3D printed scaffolds. Furthermore, this temperature and incubation period were selected to ensure the integrity of the produced scaffolds (CH destabilizes at temperatures > 40 °C [22]) as well as to grant an appropriate reduction of the GO. Finally, the obtained materials were crosslinked and air-dried, yielding TGC_irGO scaffolds. To fully disclose the possible improved bone healing properties of TGC_irGO scaffolds resulting from the presence of rGO, TGC_GO scaffolds (containing GO and not subjected to the *in situ* reduction) and TGC scaffolds (without containing GO and without being subjected to a reduction process) were also prepared.

The suitability of the *in situ* green reduction of the GO incorporated on TGC scaffolds was then analysed. The TGC_irGO scaffolds displayed a similar design and shape to that of both TGC_GO and TGC scaffolds (Fig. 1B). These results indicate that the *in situ* green reduction process is not detrimental for the macroscopic structure of the scaffolds. However, the TGC_GO scaffolds presented a dark brown colour, due to the original GO solution colour (Fig. S1C) [5]. Furthermore, the *in situ* green reduction process produced a darker TGC_irGO scaffolds (Fig. 1B). Such phenomenon is attributed to the *in situ* formation of rGO, which has a dark colour [23,24]. As a control, the direct reduction of GO with LAA was also performed (Fig. S1 C). The rGO formed in these conditions aggregated during the reduction process, which did not allow its printability (Fig. S1 C). These results further confirm the suitability of the *in situ* green reduction process for attaining 3D printed scaffolds incorporating rGO.

The surface morphology of the scaffolds was also characterized through the acquisition of SEM images. The TGC, TGC_GO and TGC_irGO scaffolds presented a similar architecture, macroporosity and roughness on their surface (Fig. 1C and Fig. S3), which provide additional anchorage points for cell attachment and proliferation [25].

3.2. Characterization of the physico-chemical properties of the scaffolds

The chemical composition of the produced scaffolds was also characterized by FTIR analysis. The spectra of the powdered scaffolds revealed the characteristic peaks of the chemical bonds present on TCP (P═O stretch at 1200 cm^{-1}) and on both Gel and CH (O–H, C–H, C═O N–H (I) and (II) stretches at 3292, 2871, 1640, 1530 and 3284 cm^{-1}, respectively) (Fig. S2 A). The peaks of the chemical groups present on GO and rGO overlap those of the other materials present on TGC_GO and TGC_irGO scaffolds, respectively (Fig. S1 B and S2 B). Thus, an EDS analysis was also performed to characterize the scaffolds composition (Table S2). When compared to the TGC scaffolds, the TGC_GO scaffolds demonstrated a higher content of carbon and a lower amount of oxygen elements (Table S2). These results corroborate the presence of GO on the TGC_GO scaffolds since this nanomaterial has a high C:O ratio of 66:34 (Table S1). Furthermore, the TGC_irGO scaffolds presented the highest and lowest content of carbon and oxygen, respectively. These results further confirm the presence of rGO in the TGC_irGO scaffolds since the former has a C:O of 80:20 (as determined by the direct reduction of GO with LAA) (Table S1). Moreover, these observations also validate the reduction capacity of the *in situ* method herein developed. As importantly, TGC_irGO and TGC_GO scaffolds presented a higher content of phosphorus and calcium when compared to the TGC scaffolds (Table S2). Such results indicate that these formulations may display an improved mineralization capacity. In fact, graphene family materials' large surface area and rough surface can promote the adsorption of biomolecules and ions (like calcium) and, consequently, improve the osteoinductivity and osteoconductivity of the 3D scaffolds [26,27]. The small content of sodium detected on scaffolds is related to the use of TPP as the crosslinking agent (Table S2).

3.3. Characterization of the mechanical properties of the scaffolds

After confirming the successful production of TGC_irGO scaffolds, the mechanical properties of this 3D structure were compared to those of TGC_GO and TGC scaffolds. The mechanical resistance is of paramount importance for scaffolds to maintain, replace or improve the bone tissue functions [28,29]. Furthermore, scaffolds' mechanical properties are also crucial to avoid problems like osteopenia due to the use of bone grafts that are stiffer than the original bones or trigger the occurrence of new fractures due to low mechanical strength [30].

Therefore, the compressive strength (C_s) and Young modulus (YM) of the 3D scaffolds were determined through a compression assay performed at dry and wet states (Fig. 2). In dry conditions, scaffolds presented high C_s values (Fig. 2A). Furthermore, TGC_irGO scaffolds presented a higher C_s value than TGC_GO and TGC scaffolds. This reinforcement on the mechanical properties of the TGC_irGO scaffolds can be explained by the presence of rGO on this material. In fact, the incorporation of rGO on matrices has been shown to improve their mechanical properties to a greater extent than GO [13]. Together these results confirm that the *in situ* green reduction method used herein can be explored to further improve the mechanical properties of scaffolds incorporating GO. At the wet state, the C_s values decreased for all the 3D printed formulations (Fig. 2A). In this condition, only TGC_irGO scaffolds present C_s values within the range displayed by the trabecular bone (2–20 MPa) [29].

Furthermore, scaffolds also displayed a higher elasticity (lower YM values) than that found in the native bone (100–2000 MPa; Fig. 2B). However, the produced scaffolds are designed to act as templates during the first phases of the bone regeneration,

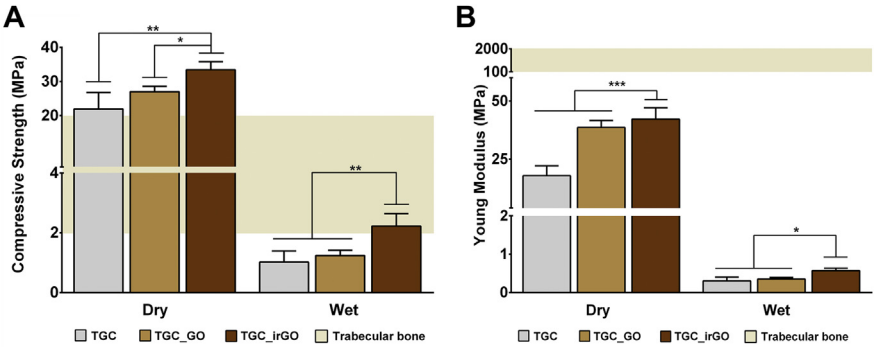

Fig. 2. Characterization of the Cs (A) and YM (B) of the produced 3D scaffolds under dry and wet conditions (data represent the mean ± standard deviation, n = 5, *p < 0.05, **p < 0.01 and ***p < 0.001). (A colour version of this figure can be viewed online.)

suffering biodegradation and replacement by the newly formed bone matrix. Such features allow scaffolds to confer a temporary support, accelerate the regeneration process, and improve the mechanical stability of the fracture site during the mineralization process [31,32].

3.4. Evaluation of the swelling profile of the 3D scaffolds

Scaffolds swelling capacity is essential for their application in bone regeneration. The absorption of fluids promotes the expansion of the polymeric matrix, leading to an increase of the scaffolds pore size, which in turn facilitates cellular internalization and the diffusion of nutrients and waste along the scaffolds structure. However, a continuous swelling must be avoided in order to prevent the loss of scaffolds' mechanical integrity as well as induce compressive stress to the surrounding tissue, causing pain to the patient [33].

The swelling behaviour of the 3D printed scaffolds was then investigated through their incubation in PBS during 12 h (Fig. 3A). The three formulations exhibited a similar behaviour, characterized by an abrupt swelling in the first 2 h, followed by a plateau phase (Fig. 3A). This behaviour is explained by the presence of hydrophilic groups (amine and hydroxyl) on the CH and Gel backbones than can be easily hydrated. Moreover, the swelling of CH involves the protonation of amine groups and mechanical relaxation of the coiled CH chains [34]. This swelling behaviour is in agreement with that of other 3D printed scaffolds prepared using polymeric materials and TCP reported in the literature [5,35].

3.5. Evaluation of the wettability surface of 3D scaffolds

The scaffolds surface wettability may influence the biological response of the implanted materials, affecting the protein adsorption and cell adhesion [36,37]. Scaffolds' surface wettability can be

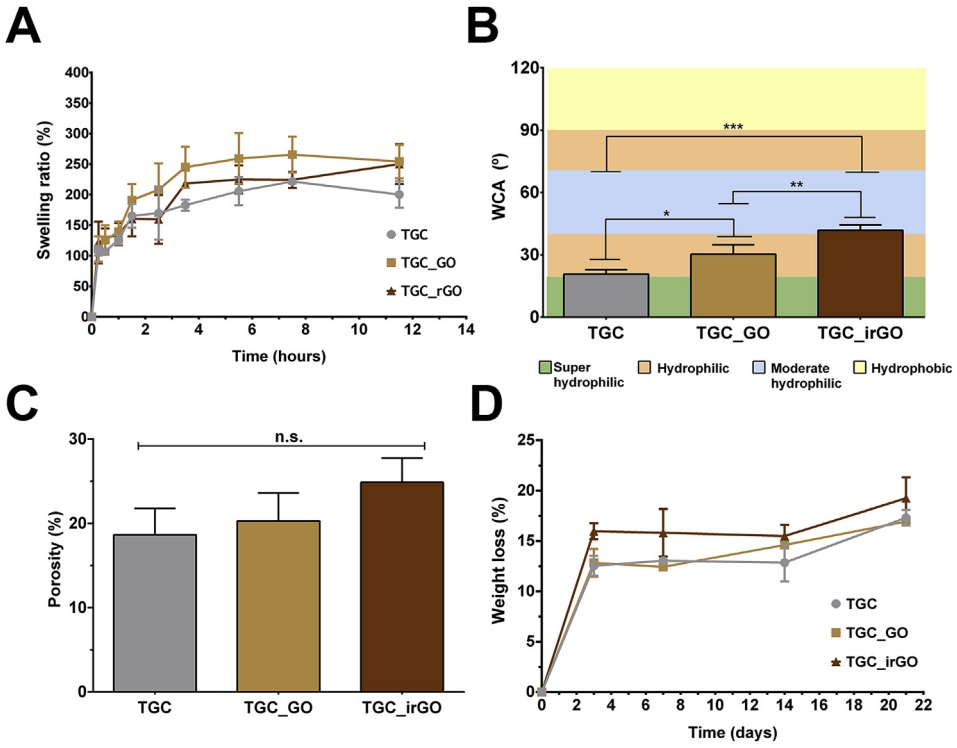

Fig. 3. Characterization of physico-chemical properties of the produced scaffolds. Characterization of scaffolds' swelling profile (A); evaluation of the scaffolds surface wettability by measuring WCA (B); evaluation of scaffolds total porosity (C); determination of scaffolds weight loss over time (D) (data represent the mean ± standard deviation, n = 5, *p < 0.05, **p < 0.01 and ***p < 0.001; the groups assigned with n.s. were not statistically significant). (A colour version of this figure can be viewed online.)

assessed through the measurement of water contact angles (WCA) [38]. In the literature, it is reported that cell adhesion is more favoured on surfaces displaying a moderate hydrophilic character ($40° < WCA < 70°$) than on hydrophobic ($WCA > 90°$) or super hydrophilic surfaces ($WCA < 20°$) [39,40].

The results obtained revealed that TGC scaffolds exhibit a WCA value of $\approx 20°$, demonstrating a super hydrophilic character. Such value is attributed to the presence of hydrophilic groups on CH and Gel backbones (Fig. 3B). However, highly hydrophilic surfaces limit or completely impair cellular attachment and spreading. In fact, cell adhesion mediating molecules bind weakly to super hydrophilic surfaces [39,41]. The TGC_GO scaffolds presented a WCA of $\approx 30°$, which can be explained by the presence of GO within the matrix. In contrast, the TGC_irGO scaffolds displayed a WCA of $\approx 42°$, which is in agreement with the presence of rGO that has a hydrophobic character. This finding indicates that TGC_irGO scaffolds present a moderate hydrophilic character, which is considered to be an optimal WCA for promoting cell adhesion and proliferation.

3.6. Evaluation of scaffolds' porosity

Scaffolds porosity has a remarkable effect on cells' infiltration, proliferation and growth. Moreover, the interconnected pores can facilitate the diffusion of Ca^{2+} and PO_4^{3-} ions throughout the scaffolds, allowing the formation of a hydroxyapatite-like layer that stimulates osteoblasts' cellular activity and the deposition of bone matrix [42].

A liquid displacement method was employed to analyse the total porosity of the scaffolds (Fig. 3C). The 3D structures displayed a total porosity of 20–30% (Fig. 3C). Even though the scaffolds total porosity is not ideal when compared to that presented by the trabecular bone (50–90%) [43], the ability of 3D structures to support cells infiltration is not solely dependent on this feature. In fact, the SEM analysis revealed that scaffolds present a suitable macroporosity: 1370 ± 290 μm for TGC scaffolds, 1463 ± 275 μm for TGC_GO scaffolds and 1232 ± 343 μm for TGC_irGO scaffolds (Fig. S3). Such values are close to the pore diameter range that is considered to be optimal for promoting cells' infiltration, new vessels' ingrowth as well as for promoting an adequate exchange of nutrients and oxygen [44]. In another work, 3D printed scaffolds containing GO also displayed a low total porosity ($\approx 35\%$) but were able to support cells' infiltration, adhesion and proliferation [5]. Furthermore, it is also worth to stress that highly porous scaffolds possess a low density and thus may have a lower mechanical strength [45,46].

3.7. Characterization of enzymatic degradation profile of the scaffolds

The biodegradation profile of the scaffolds is a crucial factor for their long-term application in bone regeneration. In this regard, scaffolds' degradation must be proportional to the new bone formation rate, without compromising the stability of the construct nor the integrity of the tissue at the injured site [47].

The degradation profile of the produced scaffolds in PBS containing lysozyme (an enzyme found in human serum) was then studied (Fig. 3D). Lysozyme mediates the hydrolyzation of the N-acetyl glucosamine groups of CH [48]. In turn, the macromolecular chains of the Gel are easily hydrolysed in the presence of water, due to their hydrophilic character [49]. The TCP suffers degradation mediated by cells and its products are naturally metabolized during the resorption bone process [35].

During the first days of incubation, all the scaffolds suffered an initial weight loss (Fig. 3D), a phenomenon that was slightly more pronounced for the TGC_irGO scaffolds. Nevertheless, TGC_irGO scaffolds degradation progressively stabilized to the values observed for TGC and TGC_GO scaffolds. Moreover, none of the scaffolds' formulations lost more than 25% of their initial weight, over a period of 21 days, indicating their suitability to be applied in bone regeneration applications.

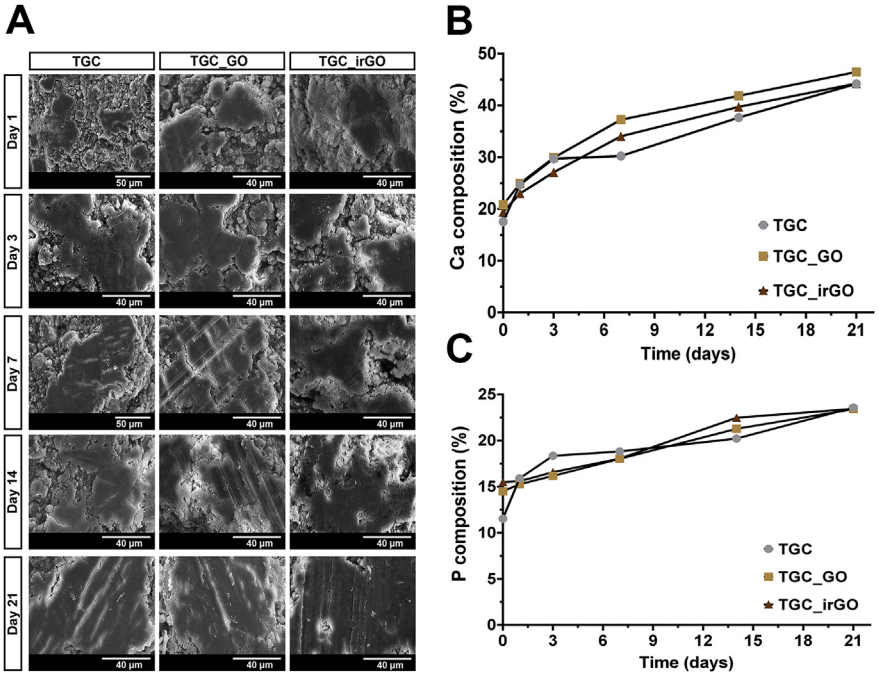

Fig. 4. Evaluation of the biomineralization at the surface of the produced scaffolds in contact with SBF. SEM images of the scaffolds surface showing the mineral deposits, after their incubation in SBF solution for 1, 3, 7, 14 and 21 days (A); EDS analysis of calcium' (B) and phosphorous (C) atomic percentages on scaffolds surfaces. (A colour version of this figure can be viewed online.)

3.8. In vitro biomineralization assay

The ability of scaffolds' surface to promote the deposition of phosphate and calcium ions in the form of hydroxyapatite crystals ($Ca_5(PO_4)_3(OH)$) is crucial for bone regeneration [50].

Thus, scaffolds biomineralization capacity was studied over a period of 21 days in SBF (Fig. 4). For this purpose, the formation of apatite crystals on the scaffolds surface was visualized through SEM analysis (Fig. 4A). EDS characterization was also performed to quantify the calcium and phosphate ions on scaffolds surface (Fig. 4B and C). The results revealed that all scaffolds formulations promoted the deposition of calcium and phosphate over time. These results can be justified by the intrinsic ability of TCP to induce the mineralization at the scaffolds' surface, increasing their bio-integration and, hence the bone regeneration process [49,51].

The extensive physico-chemical characterization performed in this study revealed that the TGC_irGO scaffolds present an improved wettability and mechanical properties in comparison to the TGC_GO and TGC scaffolds. Moreover, all scaffold formulations displayed a suitable porosity and swelling behaviour as well as adequate rates of minerals' deposition and degradation profile.

3.9. Characterization of biological properties of the scaffolds

3.9.1. Evaluation of scaffolds' cytotoxic profile

To characterize the cytotoxic profile of the produced scaffolds and their degradation products, an MTS assay was performed [29]. For this purpose, scaffolds were placed in contact with hOB cells since these cells are involved in synthesis of bone tissue ECM and have an important role in the mineralization process [50].

The results revealed that hOB cells remained viable when in contact with the scaffolds (Fig. 5A), even after 7 days of incubation. Furthermore, the optical microscopy images also demonstrated that hOB cells proliferated and exhibited an elongated and flattened morphology in contact with the scaffolds (Fig. S4). These results are in agreement with those previously reported by Serra et al., who produced 3D sponges with the same ceramic/polymeric mixture for being used in bone regeneration [17]. Moreover, TGC_irGO scaffolds exhibited a similar biocompatibility to that displayed by the TGC and TGC_GO scaffolds (Fig. 5A). This is of paramount importance since the direct administration of rGO has a cytotoxic effect on cells, which can be attributed to the low water solubility of this nano-material and also to the presence of hydrazine hydrate (a commonly used reducing agent) [14]. In this way, these results further confirm the potential of the *in situ* green reduction method, developed herein, to produce 3D printed scaffolds incorporating rGO with improved biocompatibility for bone regeneration applications.

Furthermore, hOB cells adhesion to scaffolds surface was also analysed through the acquisition of the SEM images (Fig. 5 B). Cells adhered and spread at the surface of the produced scaffolds. After 7 days, cells started to present the typical osteoblastic morphology, showing a smooth arrangement, and established connections between each other, forming a continuous cell layer. In this regard, the linear RGD-motifs of Gel may play an important role on cell adhesion [52]. As importantly, the number of hOB cells adhered on scaffolds' surface increased overtime (Fig. 5B), which further emphasizes the good biocompatibility of the produced scaffolds. Together, these results demonstrate that the 3D printed scaffolds display suitable properties for biological applications.

3.9.2. Confocal laser scanning microscopy (CLSM) analysis

The ability of cells to be internalized into the produced 3D printed scaffolds was also analysed (Fig. 6). CLSM orthogonal projections revealed that hOB cells are able to migrate into the

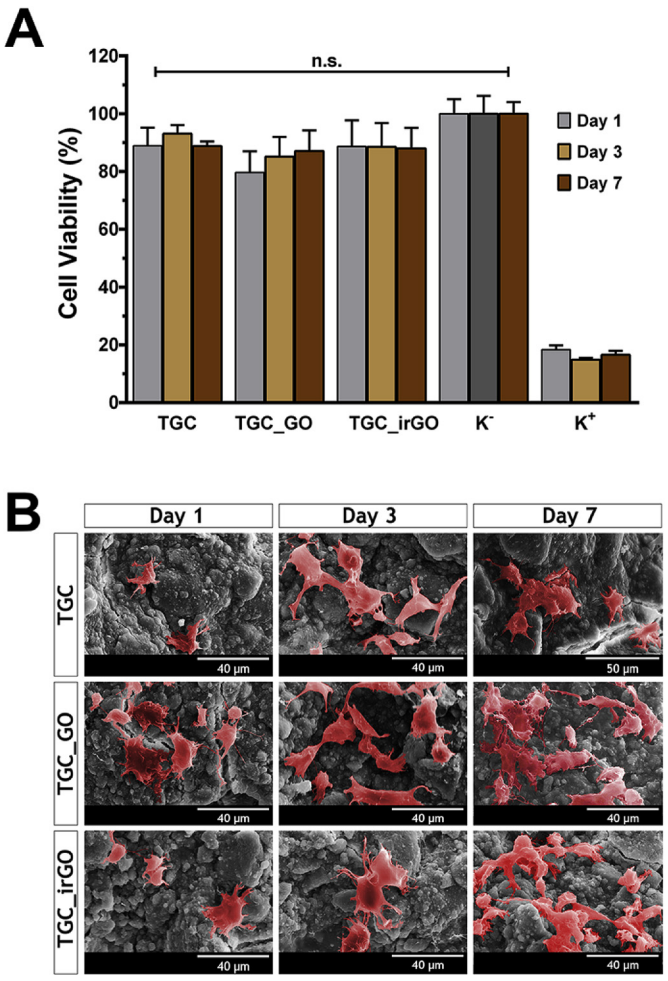

Fig. 5. Characterization of the biological properties of the scaffolds. Evaluation of the cytotoxic profile of the produced 3D scaffolds through the MTS assays at days 1, 3 and 7 (A). (K^+) positive control and (K^-) negative control were used for dead and viable cells, respectively (each result is the mean ± standard deviation, n = 5; n.s: the groups assigned with n.s. were not statistically significant); Representative pseudo-coloured SEM images of hOB cells adhered onto the surface of scaffolds over a period of 1, 3 and 7 days (B). (A colour version of this figure can be viewed online.)

scaffold's interior (Fig. 6D–F). Furthermore, the depth colour coding images also showed that the hOB cells migrated within the scaffolds porous network (Fig. 6G–L) up to a depth of 80–140 μm (coloured in blue), and the majority of the cells remain at a depth of 40–80 μm (coloured in green). In this way, the produced 3D matrices have suitable properties to allow osteoblasts growth within their structure. Such is essential to improve cells' growth and differentiation, leading to an improved deposition of new bone matrix and, consequently, to bone tissue regeneration [53].

3.9.3. Alizarin Red S (ARS) staining

The ARS staining was performed to evaluate the matrix mineralization activity performed by hOB cells incubated with the scaffolds [54]. For this purpose, optical microscopic images of the mineralized matrix produced by hOB cells in contact with the scaffolds during 1, 3, 7, 14 and 21 days were acquired (Fig. 7A). Furthermore, the calcium deposits produced by the hOB cells on scaffolds' structure were quantified following the ARS assay protocol (Fig. 7B) [5].

For all the produced scaffolds, the determined ARS concentration increased along time (Fig. 7B), revealing that the calcium

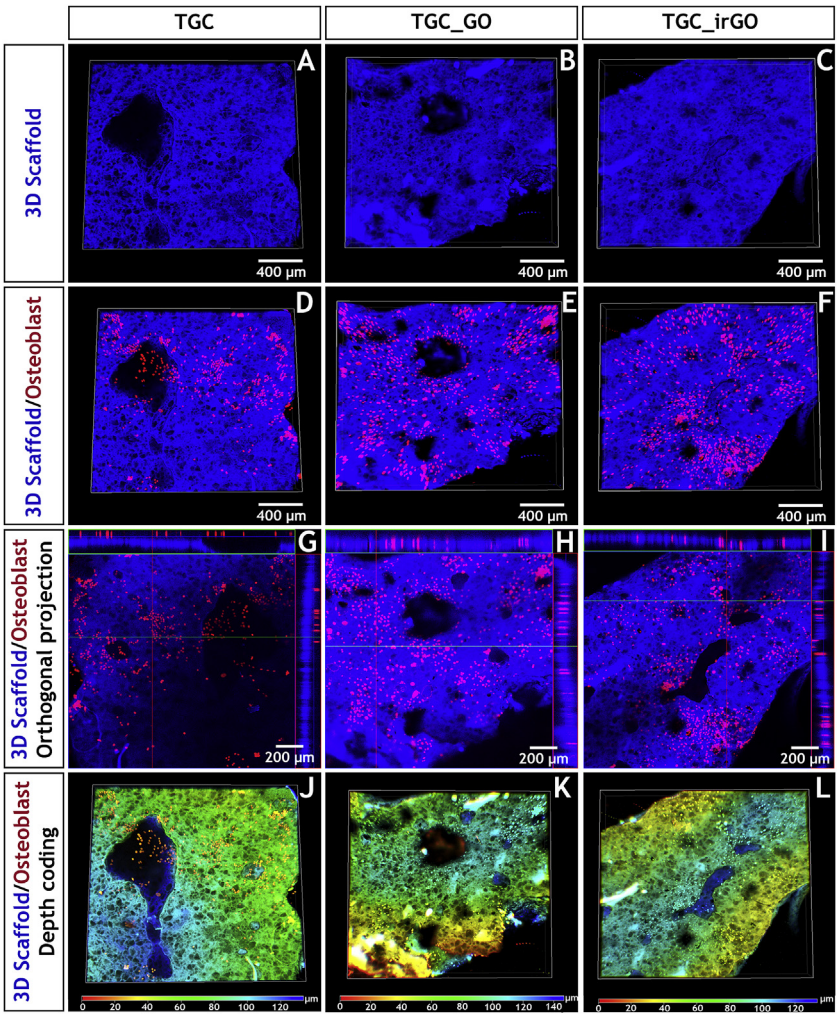

Fig. 6. CLSM images acquired to characterize cell internalization within the TGC, TGC_GO and TGC_irGO scaffolds. 3D reconstruction images (A–F) and orthogonal projections (G–I) of the cells in contact with the scaffolds. Depth colour coding CLSM images of the scaffolds are also presented (J–L). (A colour version of this figure can be viewed online.)

deposition is promoted on scaffolds surface. Particularly, the TGC_irGO scaffolds presented a higher ARS concentration after 21 days of incubation (≈27 mg/mL) when compared to TGC_GO (≈23 mg/mL) and TGC (≈22 mg/mL) scaffolds (Fig. 7B). These values are also superior to those reported in literature for β-TCP/alginic acid/GO scaffolds (≈14 mg/mL; 21 days incubation period [5]) or CH/Gel/β-TCP sponges (≈0.6 mg/mL; 14 days incubation period [17]). Such improved calcium deposition mediated by TGC_irGO scaffolds is in agreement with literature reports where the same behaviour was observed for matrices incorporating rGO [55,56]. Kanayama et al. reported that collagen films coated with rGO displayed a higher calcium adsorption than their equivalents containing GO [13]. The deposition of calcium at scaffolds' surface reflects their osteogenic capacity, which is important for bone tissue regeneration applications [57]. The results herein obtained also disclosed that the *in situ* green reduction method can yield 3D printed scaffolds incorporating rGO with an enhanced biomineralization activity.

3.9.4. Determination of the alkaline phosphatase (ALP) activity

ALP is an important early osteogenic and biochemical marker of osteoblasts' differentiation [58]. Furthermore, the ALP is involved in the cleavage of organic phosphate, providing calcium and phosphate ions that are essential for the mineralization process of the bone matrix [59]. For this purpose, the ALP activity of hOB cells in contact with the 3D scaffolds (normalized to the dsDNA concentration) was measured along time (Fig. 7C).

Overall, hOB cells incubated with TGC_GO and TGC_irGO scaffolds presented a higher ALP activity than those incubated with the TGC scaffolds (Fig. 7C). After 14 days of incubation, cells in contact with TGC_GO or with TGC_irGO scaffolds displayed a 1.6 and 1.9-fold higher ALP activity, respectively, than those in contact with TGC scaffolds (Fig. 7C). These results are also in agreement with the ARS assays, in which the TGC_irGO scaffolds exhibited an improved calcium deposition. In fact, Ca^{2+} can stimulate ALP activity and matrix mineralization [60].

3.9.5. Evaluation of the bactericidal activity of the scaffolds

Bone implants failures are prompted by bacterial infections caused by microorganisms, that induce the formation of biofilms on the surface of the implants. These biofilms can compromise the successful application and function of these devices. Moreover, bacterial infections lead to prolonged hospitalization periods, increased costs, and in extreme cases, patient death [61].

Therefore, the antibacterial activity of the produced scaffolds against *S. aureus* and *E. coli* was screened through an agar diffusion method. The 3D printed scaffolds were able to inhibit the *S. aureus* and *E. coli* growth (Fig. 8 and Fig. S5). Moreover, the SEM analysis

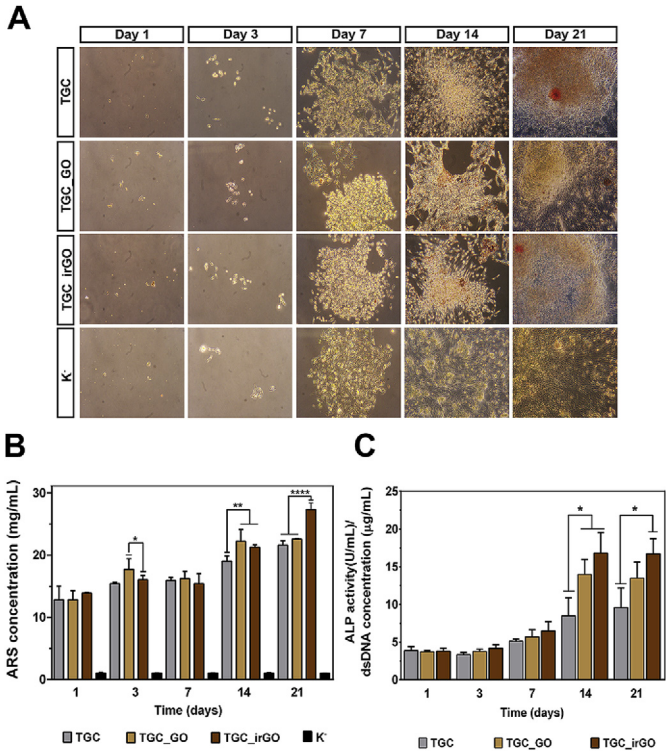

Fig. 7. Characterization of the osteogenic properties of the produced scaffolds. Optical microscopy images of hOB cells stained with Alizarin Red S after 1, 3, 7, 14 and 21 days of incubation with TGC, TGC_GO and TGC_irGO scaffolds (A); Determination of the Alizarin Red concentration (B) and ALP activity (C) of hOB cells cultured in the presence of the 3D scaffolds after 1, 3, 7, 14 and 21 days of incubation (each result is the mean ± standard deviation, n = 6, *p < 0.05, **p < 0.01 and ****p < 0.0001; the groups not signed with * were not statistically significant). (A colour version of this figure can be viewed online.)

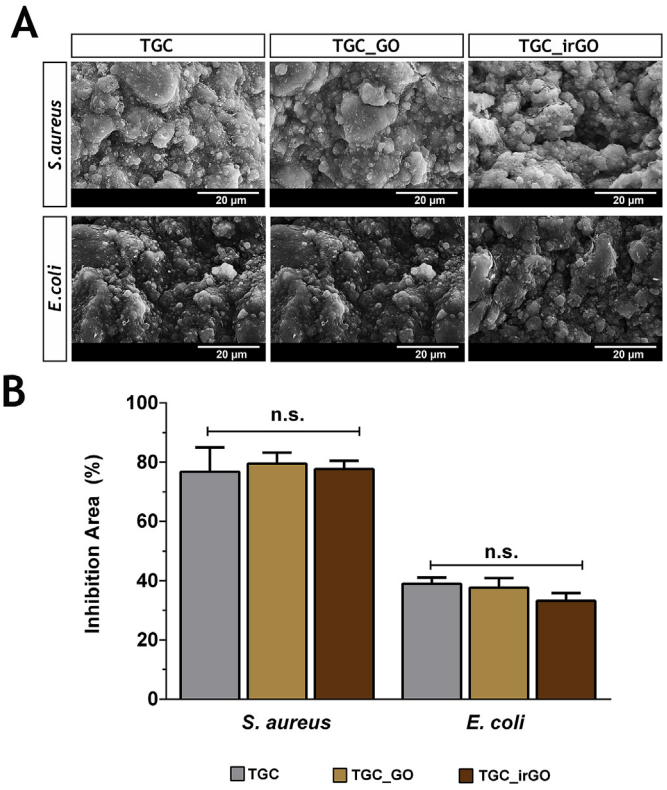

Fig. 8. Characterization of the antimicrobial activity of the produced scaffolds. SEM images of scaffolds surface after being in contact with *S. aureus* and *E. coli* (A); Analysis of the inhibition area obtained for scaffolds in contact with *S. aureus* and *E. coli* strains (B) (each result is presented in percentage and is the mean ± standard deviation, n = 3; the groups assigned with n.s. were not statistically significant). (A colour version of this figure can be viewed online.)

also revealed that no biofilm formation occurred at the scaffolds surface when they are incubated with either of the two microorganisms (Fig. 8A). In contrast, biofilm formation was noticed in the control samples, where bacteria were seeded in contact with agar plate (without the scaffolds) (Fig. S6). Such results can be explained by the presence of the CH in all scaffolds' formulations, which is widely described in the literature as a polymer with antibacterial activity [17,18,35]. CH can disturb the bacterial growth through the interaction of its positively charged amine groups with the electronegative residues present at bacterial cell wall surface, which increase cell wall permeability and, subsequently, the leakage of intracellular constituents, leading to dissipation of ionic gradients within the bacteria. Furthermore, CH can also form a barrier on the surface of the bacteria, preventing nutrients from entering into the bacteria [62].

Scaffolds displayed a more pronounced antibacterial activity against *S. aureus* (Fig. 8B and Fig. S5). The differential inhibitory activity of the CH present on scaffolds towards *S.aureus* and *E.coli* is likely to occur due to the high complexity and thickness of the Gram-negative bacteria (*E. coli*) cell wall. The presence of an outer membrane in the Gram-negative bacteria provides a barrier against polymeric macromolecules, hindering the diffusion of CH [63].

4. Conclusions

In this work, a novel method was developed to perform the *in situ* green-reduction of the GO incorporated on 3D printed scaffolds. The results revealed that TGC_irGO scaffolds retain their initial structure upon reduction. Furthermore, TGC_irGO scaffolds presented an enhanced wettability and mechanical properties, without impairing their porosity, when compared to their equivalents functionalized with GO (TGC_GO) and non-functionalized scaffolds (TGC). Moreover, the TGC_irGO scaffolds displayed an improved calcium deposition at their surface and were able to augment the ALP activity, along 21 days of incubation. Additionally, scaffolds also exhibited antimicrobial properties against *S. aureus* and *E. coli*, without compromising the viability and proliferation of osteoblasts. Overall, these results reveal the improved potential of TGC_irGO scaffolds for bone repair and validate the developed *in situ* green reduction protocol. In a near future, complementary assays (e.g. determination of osteopontin, osteocalcin and BMP-2 expression) may be performed to evaluate the osteoinductive and osteoconductive potential of the TGC_irGO scaffolds. Furthermore, *in vivo* assays may be pursued in order to fully depict the potential of the scaffolds for bone regeneration (e.g. bone matrix production and mineralization). Additionally, the incorporation of bioactive molecules (e.g. growth factors and bone morphogenic proteins) in TGC_irGO scaffolds and the use of more advanced 3D printing techniques can be hypothesized to further improve the bone healing process and to assemble 3D structures with a higher resolution, respectively.

Acknowledgements

The authors would like to acknowledge Professor Abílio Silva for the help with the mechanical assays. This work was supported by FEDER funds through the POCI– COMPETE 2020 – Operational

Programme Competitiveness and Internationalisation in Axis I – Strengthening research, technological development and innovation (Project POCI-01-0145-FEDER-007491) and National Funds by FCT – Foundation for Science and Technology (Project UID/ Multi/ 00709/2013). The funding from CENTRO-01-0145-FEDER-028989 is also acknowledged. Sónia P. Miguel and Duarte de Melo-Diogo acknowledge individual PhD fellowships from FCT (SFRH/BD/ 109563/2015 and SFRH/BD/103506/2014).

Appendix A. Supplementary data

Supplementary data to this article can be found online at https://doi.org/10.1016/j.carbon.2019.01.100.

References

[1] S. Pei, H.-M. Cheng, The reduction of graphene oxide, Carbon 50 (9) (2012) 3210–3228.
[2] H. Shen, L. Zhang, M. Liu, Z. Zhang, Biomedical applications of graphene, Theranostics 2 (3) (2012) 283–294.
[3] D. de Melo-Diogo, E.C. Costa, C.G. Alves, R. Lima-Sousa, P. Ferreira, R.O. Louro, I.J. Correia, POxylated graphene oxide nanomaterials for combination chemo-phototherapy of breast cancer cells, Eur. J. Pharm. Biopharm. 131 (2018) 162–169.
[4] S. Neto, D. de Melo-Diogo, I. Correia, C. Paquete, R. Louro, Characterization of OmcA mutants from shewanella oneidensis MR-1 to investigate the molecular mechanisms underpinning electron transfer across the microbe-electrode interface, Fuel Cells 17 (5) (2017) 601–611.
[5] J.C. Boga, S.P. Miguel, D. de Melo-Diogo, A.G. Mendonça, R.O. Louro, I.J. Correia, In vitro characterization of 3D printed scaffolds aimed at bone tissue regeneration, Colloids Surfaces B Biointerfaces 165 (2018) 207–218.
[6] S. Dinescu, M. Ionita, A.M. Pandele, B. Galateanu, H. Iovu, A. Ardelean, M. Costache, A. Hermenean, In vitro cytocompatibility evaluation of chitosan/graphene oxide 3D scaffold composites designed for bone tissue engineering, Bio Med. Mater. Eng. 24 (6) (2014) 2249–2256.
[7] M. Nair, D. Nancy, A.G. Krishnan, G. Anjusree, S. Vadukumpully, S.V. Nair, Graphene oxide nanoflakes incorporated gelatin–hydroxyapatite scaffolds enhance osteogenic differentiation of human mesenchymal stem cells, Nanotechnology 26 (16) (2015) 161001.
[8] D. de Melo-Diogo, C. Pais-Silva, E.C. Costa, R.O. Louro, I.J. Correia, D-α-tocopheryl polyethylene glycol 1000 succinate functionalized nanographene oxide for cancer therapy, Nanomedicine 12 (5) (2017) 443–456.
[9] Q. Chen, J.D. Mangadlao, J. Wallat, A. De Leon, J.K. Pokorski, R.C. Advincula, 3D printing biocompatible polyurethane/poly (lactic acid)/graphene oxide nanocomposites: Anisotropic properties, ACS Appl. Mater. Interfaces 9 (4) (2017) 4015–4023.
[10] T.R. Correia, D.R. Figueira, K.D. de Sá, S.P. Miguel, R.G. Fradique, A.G. Mendonça, I.J. Correia, 3D printed scaffolds with bactericidal activity aimed for bone tissue regeneration, Int. J. Biol. Macromol. 93 (2016) 1432–1445.
[11] Y. Liu, F. Zhu, H. Zhu, Review on techniques of design and manufacturing for bone tissue engineering scaffold, in: Biomedical Engineering and Informatics, 2009. BMEI'09. 2nd International Conference on, IEEE, 2009, pp. 1–4.
[12] V.C. Sanchez, A. Jachak, R.H. Hurt, A.B. Kane, Biological interactions of graphene-family nanomaterials: An interdisciplinary review, Chem. Res. Toxicol. 25 (1) (2011) 15–34.
[13] I. Kanayama, H. Miyaji, H. Takita, E. Nishida, M. Tsuji, B. Fugetsu, L. Sun, K. Inoue, A. Ibara, T. Akasaka, Comparative study of bioactivity of collagen scaffolds coated with graphene oxide and reduced graphene oxide, Int. J. Nanomed. 9 (2014) 3363–3373.
[14] D. de Melo-Diogo, R. Lima-Sousa, C.G. Alves, E.C. Costa, R.O. Louro, I.J. Correia, Functionalization of graphene family nanomaterials for application in cancer therapy, Colloids Surfaces B Biointerfaces 171 (2018) 260–275.
[15] S. Stankovich, D.A. Dikin, R.D. Piner, K.A. Kohlhaas, A. Kleinhammes, Y. Jia, Y. Wu, S.T. Nguyen, R.S. Ruoff, Synthesis of graphene-based nanosheets via chemical reduction of exfoliated graphite oxide, Carbon 45 (7) (2007) 1558–1565.
[16] M.J. Fernández-Merino, L. Guardia, J. Paredes, S. Villar-Rodil, P. Solís-Fernández, A. Martínez-Alonso, J. Tascon, Vitamin C is an ideal substitute for hydrazine in the reduction of graphene oxide suspensions, J. Phys. Chem. C 114 (14) (2010) 6426–6432.
[17] I. Serra, R. Fradique, M. Vallejo, T. Correia, S. Miguel, I. Correia, Production and characterization of chitosan/gelatin/β-TCP scaffolds for improved bone tissue regeneration, Mater. Sci. Eng. C 55 (2015) 592–604.
[18] S.P. Miguel, M.P. Ribeiro, H. Brancal, P. Coutinho, I.J. Correia, Thermoresponsive chitosan–agarose hydrogel for skin regeneration, Carbohydr. Polym. 111 (2014) 366–373.
[19] J.L. Moreau, H.H.K. Xu, Mesenchymal stem cell proliferation and differentiation on an injectable calcium phosphate-chitosan composite scaffold, Biomaterials 30 (14) (2009) 2675–2682.
[20] R. Fradique, T.R. Correia, S. Miguel, K. De Sa, D. Figueira, A. Mendonça, I. Correia, Production of new 3D scaffolds for bone tissue regeneration by rapid prototyping, J. Mater. Sci. Mater. Med. 27 (4) (2016) 69.
[21] D. Choi, P.N. Kumta, Mechano-chemical synthesis and characterization of nanostructured β-TCP powder, Mater. Sci. Eng. C 27 (3) (2007) 377–381.
[22] E. Szymańska, K. Winnicka, Stability of chitosan—a challenge for pharmaceutical and biomedical applications, Mar. Drugs 13 (4) (2015) 1819–1846.
[23] K. Yang, J. Wan, S. Zhang, B. Tian, Y. Zhang, Z. Liu, The influence of surface chemistry and size of nanoscale graphene oxide on photothermal therapy of cancer using ultra-low laser power, Biomaterials 33 (7) (2012) 2206–2214.
[24] R. Lima-Sousa, D. de Melo-Diogo, C.G. Alves, E.C. Costa, P. Ferreira, R.O. Louro, I.J. Correia, Hyaluronic acid functionalized green reduced graphene oxide for targeted cancer photothermal therapy, Carbohydr. Polym. 200 (2018) 93–99.
[25] J. Mitra, G. Tripathi, A. Sharma, B. Basu, Scaffolds for bone tissue engineering: role of surface patterning on osteoblast response, RSC Adv. 3 (28) (2013) 11073–11094.
[26] T. Alava, J.A. Mann, C.c. Théodore, J.J. Benitez, W.R. Dichtel, J.M. Parpia, H.G. Craighead, Control of the graphene–protein interface is required to preserve adsorbed protein function, Anal. Chem. 85 (5) (2013) 2754–2759.
[27] J.S. Park, N.-I. Goo, D.-E. Kim, Mechanism of DNA adsorption and desorption on graphene oxide, Langmuir 30 (42) (2014) 12587–12595.
[28] L. Polo-Corrales, M. Latorre-Esteves, J.E. Ramirez-Vick, Scaffold design for bone regeneration, J. Nanosci. Nanotechnol. 14 (1) (2014) 15–56.
[29] S. Bose, M. Roy, A. Bandyopadhyay, Recent advances in bone tissue engineering scaffolds, Trends Biotechnol. 30 (10) (2012) 546–554.
[30] K.J. Burg, S. Porter, J.F. Kellam, Biomaterial developments for bone tissue engineering, Biomaterials 21 (23) (2000) 2347–2359.
[31] S.C. Miranda, G.A. Silva, R.C. Hell, M.D. Martins, J.B. Alves, A.M. Goes, Three-dimensional culture of rat BMMSCs in a porous chitosan-gelatin scaffold: A promising association for bone tissue engineering in oral reconstruction, Arch. Oral Biol. 56 (1) (2011) 1–15.
[32] L. Bi, W. Cheng, H. Fan, G. Pei, Reconstruction of goat tibial defects using an injectable tricalcium phosphate/chitosan in combination with autologous platelet-rich plasma, Biomaterials 31 (12) (2010) 3201–3211.
[33] L. Tao, L. Zhonglong, X. Ming, Y. Zezheng, L. Zhiyuan, Z. Xiaojun, W. Jinwu, In vitro and in vivo studies of a gelatin/carboxymethyl chitosan/LAPONITE® composite scaffold for bone tissue engineering, RSC Adv. 7 (85) (2017) 54100–54110.
[34] W. Thein-Han, R. Misra, Biomimetic chitosan–nanohydroxyapatite composite scaffolds for bone tissue engineering, Acta Biomater. 5 (4) (2009) 1182–1197.
[35] K.D. De Sá, D.R. Figueira, S.P. Miguel, T.R. Correia, A.P. Silva, I.J. Correia, 3D scaffolds coated with nanofibers displaying bactericidal activity for bone tissue applications, Int. J. Polym. Mater. Biomater 66 (9) (2017) 432–442.
[36] J. Wei, T. Igarashi, N. Okumori, T. Igarashi, T. Maetani, B. Liu, M. Yoshinari, Influence of surface wettability on competitive protein adsorption and initial attachment of osteoblasts, Biomed. Mater. 4 (4) (2009), 045002.
[37] S. Guo, X. Zhu, M. Li, L. Shi, J.L.T. Ong, D. Janczewski, K.G. Neoh, Parallel control over surface charge and wettability using polyelectrolyte architecture: Effect on protein adsorption and cell adhesion, ACS Appl. Mater. Interfaces 8 (44) (2016) 30552–30563.
[38] G.S. Diogo, V.M. Gaspar, I.R. Serra, R. Fradique, I.J. Correia, Manufacture of β-TCP/alginate scaffolds through a Fab@home model for application in bone tissue engineering, Biofabrication 6 (2) (2014), 025001.
[39] S.M. Oliveira, N.M. Alves, J.F. Mano, Cell interactions with superhydrophilic and superhydrophobic surfaces, J. Adhes. Sci. Technol. 28 (8–9) (2014) 843–863.
[40] D.P. Dowling, I.S. Miller, M. Ardhaoui, W.M. Gallagher, Effect of surface wettability and topography on the adhesion of osteosarcoma cells on plasma-modified polystyrene, J. Biomater. Appl. 26 (3) (2011) 327–347.
[41] L. Bacakova, E. Filova, M. Parizek, T. Ruml, V. Svorcik, Modulation of cell adhesion, proliferation and differentiation on materials designed for body implants, Biotechnol. Adv. 29 (6) (2011) 739–767.
[42] S.J. Hollister, Porous scaffold design for tissue engineering, Nat. Mater. 4 (7) (2005) 518–524.
[43] C. Torres-Sanchez, F. Al Mushref, M. Norrito, K. Yendall, Y. Liu, P.P. Conway, The effect of pore size and porosity on mechanical properties and biological response of porous titanium scaffolds, Mater. Sci. Eng. C 77 (2017) 219–228.
[44] X. Xiao, W. Wang, D. Liu, H. Zhang, P. Gao, L. Geng, Y. Yuan, J. Lu, Z. Wang, The promotion of angiogenesis induced by three-dimensional porous beta-tricalcium phosphate scaffold with different interconnection sizes via activation of PI3K/Akt pathways, Sci. Rep. 5 (2015) 9409.
[45] H.R. Ramay, M. Zhang, Preparation of porous hydroxyapatite scaffolds by combination of the gel-casting and polymer sponge methods, Biomaterials 24 (19) (2003) 3293–3302.
[46] V. Karageorgiou, D. Kaplan, Porosity of 3D biomaterial scaffolds and osteogenesis, Biomaterials 26 (27) (2005) 5474–5491.
[47] F.J. O'brien, Biomaterials & scaffolds for tissue engineering, Mater. Today 14 (3) (2011) 88–95.
[48] S.P. Miguel, M.P. Ribeiro, P. Coutinho, I.J. Correia, Electrospun polycaprolactone/aloe Vera_Chitosan nanofibrous asymmetric membranes aimed for wound healing applications, Polymers 9 (5) (2017) 183.
[49] M. Peter, N. Ganesh, N. Selvamurugan, S. Nair, T. Furuike, H. Tamura, R. Jayakumar, Preparation and characterization of chitosan–gelatin/nanohydroxyapatite composite scaffolds for tissue engineering applications, Carbohydr. Polym. 80 (3) (2010) 687–694.

[50] H.C. Blair, Q.C. Larrouture, Y. Li, H. Lin, D. Beer-Stoltz, L. Liu, R.S. Tuan, L.J. Robinson, P.H. Schlesinger, D.J. Nelson, Osteoblast differentiation and bone matrix formation in vivo and in vitro, Tissue Eng. B Rev. 23 (3) (2017) 268–280.
[51] Y. Zhou, H. Yao, J. Wang, D. Wang, Q. Liu, Z. Li, Greener synthesis of electrospun collagen/hydroxyapatite composite fibers with an excellent microstructure for bone tissue engineering, Int. J. Nanomed. 10 (2015) 3203–3215.
[52] N. Davidenko, C.F. Schuster, D.V. Bax, R.W. Farndale, S. Hamaia, S.M. Best, R.E. Cameron, Evaluation of cell binding to collagen and gelatin: A study of the effect of 2D and 3D architecture and surface chemistry, J. Mater. Sci. Mater. Med. 27 (10) (2016) 148.
[53] S. Liao, F. Cui, Y. Zhu, Osteoblasts adherence and migration through three-dimensional porous mineralized collagen based composite: nHAC/PLA, J. Bioact. Compat Polym. 19 (2) (2004) 117–130.
[54] P. Vashisth, J.R. Bellare, Development of hybrid scaffold with biomimetic 3D architecture for bone regeneration, Nanomed. Nanotechnol. Biol. Med. 14 (4) (2018) 1325–1336.
[55] M. Mehrali, E. Moghaddam, S.F.S. Shirazi, S. Baradaran, M. Mehrali, S.T. Latibari, H.S.C. Metselaar, N.A. Kadri, K. Zandi, N.A.A. Osman, Synthesis, mechanical properties, and in vitro biocompatibility with osteoblasts of calcium silicate–reduced graphene oxide composites, ACS Appl. Mater. Interfac. 6 (6) (2014) 3947–3962.
[56] J.H. Lee, Y.C. Shin, S.-M. Lee, O.S. Jin, S.H. Kang, S.W. Hong, C.-M. Jeong, J.B. Huh, D.-W. Han, Enhanced osteogenesis by reduced graphene oxide/hydroxyapatite nanocomposites, Sci. Rep. 5 (2015) 18833.
[57] A. Marrella, G. Tedeschi, P. Giannoni, A. Lagazzo, F. Sbrana, F. Barberis, R. Quarto, F. Puglisi, S. Scaglione, "Green-reduced" graphene oxide induces in vitro an enhanced biomimetic mineralization of polycaprolactone electrospun meshes, Mater. Sci. Eng. C 93 (2018) 1044–1053.
[58] X. Zhang, W. Chang, P. Lee, Y. Wang, M. Yang, J. Li, S.G. Kumbar, X. Yu, Polymer-ceramic spiral structured scaffolds for bone tissue engineering: Effect of hydroxyapatite composition on human fetal osteoblasts, PLoS One 9 (1) (2014), e85871.
[59] J.B. Lee, J.E. Kim, M.S. Bae, S.A. Park, D.A. Balikov, H.-j. Sung, H.B. Jeon, H.K. Park, S.H. Um, K.S. Lee, Development of poly (ε-caprolactone) scaffold loaded with simvastatin and beta-cyclodextrin modified hydroxyapatite inclusion complex for bone tissue engineering, Polymers 8 (2) (2016) 49.
[60] S. Maeno, Y. Niki, H. Matsumoto, H. Morioka, T. Yatabe, A. Funayama, Y. Toyama, T. Taguchi, J. Tanaka, The effect of calcium ion concentration on osteoblast viability, proliferation and differentiation in monolayer and 3D culture, Biomaterials 26 (23) (2005) 4847–4855.
[61] S. Channasanon, P. Udomkusonsri, S. Chantaweroad, P. Tesavibul, S. Tanodekaew, Gentamicin released from porous scaffolds fabricated by stereolithography, J. Healthc. Eng. 2017 (2017).
[62] D. Simões, S.P. Miguel, M.P. Ribeiro, P. Coutinho, A.G. Mendonça, I.J. Correia, Recent advances on antimicrobial wound dressing: A review, Eur. J. Pharm. Biopharm. 127 (2018) 130–141.
[63] I. Helander, E.-L. Nurmiaho-Lassila, R. Ahvenainen, J. Rhoades, S. Roller, Chitosan disrupts the barrier properties of the outer membrane of gram-negative bacteria, Int. J. Food Microbiol. 71 (2–3) (2001) 235–244.